Electrochemical and Mechanistic Study of Oxidative Degradation of Favipiravir by Electro-generated Superoxide through Proton-coupled Electron Transfer

Tatsushi Nakayama,[*,†] *and Ryo Honda,*[‡]

† Gifu Pharmaceutical University, 1-25-4 Daigaku-nishi, Gifu, 501-1196, Japan

‡ United Graduate School of Drug Discovery and Medical Information Sciences, Gifu University, 1-1 Yanagido, Gifu, 501-1193, Japan

*Phone: +81-58-230-8100 Fax: +81-58-230-8200 E-mail: tnakayama@gifu-pu.ac.jp

ABSTRACT

Electrochemical analyses aided by density functional theory calculations were used to investigate the oxidative degradation of pyrazine antiviral drugs, 3-hydroxypyrazine-2-carboxamide (T-1105) and 6-fluoro-3-hydroxypyrazine-2-carboxamide (favipiravir, T-705), by electro-generated superoxide radical anion ($O_2^{\bullet-}$). T-1105 and T-705 are antiviral RNA nucleobase analogs that selectively inhibit the RNA-dependent RNA polymerase. They are expected as a drug candidate against various viral infections, including COVID-19. The pyrazine moiety was decomposed by $O_2^{\bullet-}$ through proton-coupled electron transfer (PCET). Our results show that its active form,

pyrazine-ribofuranosyl-5'-triphosphate, is easily oxidized under inflamed organs by overproduced $O_2^{\bullet-}$ through the PCET mechanism in the immune system. This mechanistic study implies that the oxidative degradation of pyrazine derivatives will be prevented by controlling the PCET through simple modification of the pyrazine structure.

KEYWORDS: superoxide radical anion; avigan; SARS-CoV-2; proton-coupled electron transfer; inflammatory; density functional theory

1 INTRODUCTION

The development of therapeutic medicines against the newly pathogenic severe acute respiratory syndrome coronavirus 2 (SARS-CoV-2) is desired considering the current COVID-19 pandemic.[1] However, developing a highly efficient antiviral drug against a new virus in which virus-type mutations occur frequently or whose characteristics are unknown properties is difficult. Therefore, using existing antiviral drugs with a broad spectrum and certain effectiveness for various viruses is currently the first choice for effective drug therapy. To identify a promising candidate drug to treat viral infection, especially for influenza, hepatitis C, and now COVID-19, several RNA nucleobase analogs such as remdesivir,[2,3] ribavirin,[4] brincidofovir,[5] and favipiravir: 6-fluoro-3-hydroxypyrazine-2-carboxamide (favipiravir, T-705), sold under the brand name avigan,[6] have been developed.

Pyrazine derivatives such as T-705,[7–9] 3-hydroxypyrazine-2-carboxamide (T-1105),[10,11] and 3,4-dihydro-3-oxo-4-β-d-ribofuranosyl-2-pyrazinecarboxamide (T-1106),[12] blocks the replication of many RNA viruses, including arenaviruses (Junin, Machupo, and Pichinde), and are expected to be an effective antiviral drug for COVID-19. The selective inhibition of viral RNA-dependent RNA polymerase (RdRp) is assumed to be the mechanism of action for their anti-SARS-CoV-

2.[13,14] Their antiviral effects are based on the fact that the viral RNA polymerase mistakenly recognizes 3-hydroxypyrazine-2-carboxamide-ribofuranosyl-5'-triphosphate (pyrazine-RTP) structure as a purine nucleotide (adenosine and guanosine). Thus, they prevent virus multiplication with purine analog effects as RdRp inhibitors. Since RdRp domains are not present in human cells and are conserved among RNA viruses, this distinct specific mechanism targeting RNA viral polymerases makes pyrazine derivatives an attractive drug candidate.

Chart 1. Structures of the Antiviral Drugs Considered in This Study

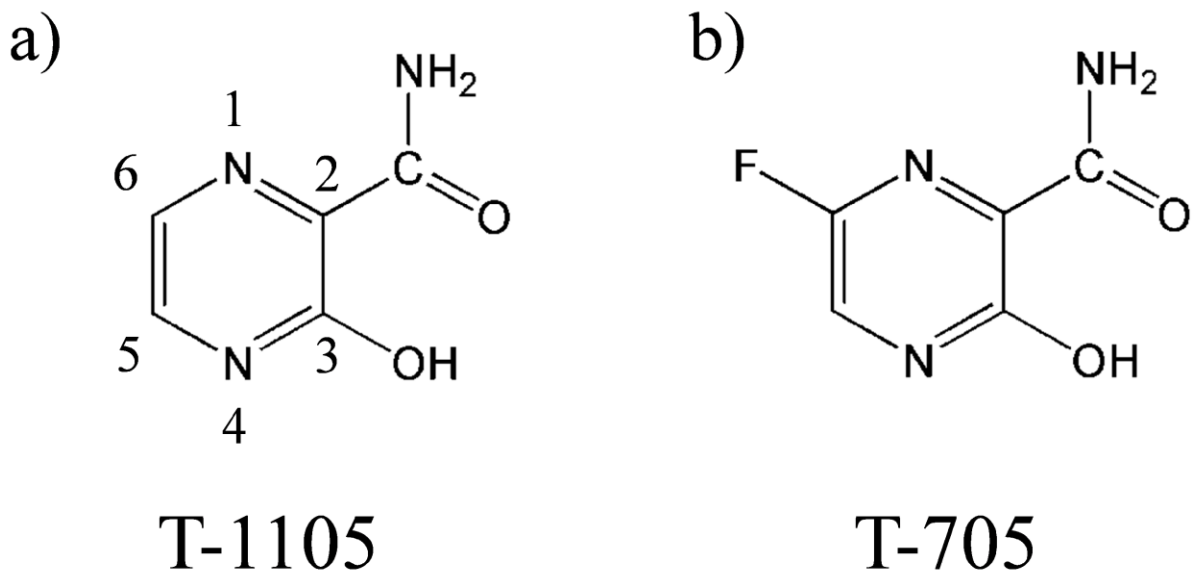

a) 3-hydroxypyrazine-2-carboxamide (T-1105), and b) 6-fluoro-3-hydroxypyrazine-2-carboxamide (favipiravir; T-705)

With its mechanism of action and a broad range of antiviral activity, the pyrazine-structural drugs (T-1105, or its more active derivative: T-705) are promising drug candidates for RNA viral diseases, including COVID-19. T-705 is now expected to conduct clinical trials for use against COVID-19 worldwide; although there left a fatal issue that the antiviral effect is weak in vivo, a high dose is needed for potential antiviral activity.[15] T-1105 is a prodrug, which needs to be metabolized to its active form, pyrazine-RTP.[11] Then, pyrazine-RTP prevent virus multiplication

by their analog effect but cannot kill the virus.[11,16] Therefore, the immune response must be used to kill the virus while also preventing it from multiplying.[17] Considering these biological conditions for its mechanism of action in vivo, the effective concentration of its active form after the metabolization will be lower, although T-705 is available in both oral and intravenous formulations.[7,9,11] Regarding the favipiravir as a prodrug of the RNA polymerase inhibitor, the purpose is to supply favipiravir-RTP; the active form is a purine nucleic acid analog vicinity of the virus in inflamed organs such as the lung. However, if most of the dosed T-705 is decomposed during the conversion processes to the active form and drug delivery, the concentration near the virus drops to a level where the desired antiviral effect cannot be obtained. Therefore, if the concentration of T-705-RTP can be increased by inhibiting T-705 metabolic degradation, the antiviral efficacy can be enhanced.[9]

COVID-19 has characteristic symptoms caused by SARS-CoV-2. While most cases result in mild symptoms, some progress to viral pneumonia and multi-organ failure.[2,4,18,19] Although the mechanism of COVID-19 pneumonia is still being researched, the SARS-CoV-2 virus, like other viral pneumonia, proliferates in the lung tissue at the early stage of infection, and inflammatory symptoms in the lung appear due to the action of the immune system. As the alveolar disease progresses, respiratory failure develops, and death may follow. It is speculated that the rapid proliferation of virus causes the most alarming acute respiratory distress syndrome in the lungs and the excessive response of the immune system to the virus, causing respiratory failure and subsequent septic shock or multi-organ failure in the later stages of severe COVID-19, known as a cytokine storm.[18] To prevent this serious symptom, it is necessary to prevent the proliferation of SARS-CoV-2 and suppress the immune reaction that causes inflammation. As a drug therapy, it is highly possible that an RNA replication inhibitor such as T-705 alone cannot have an

immediate effect because it can stop the multiplication of SARS-CoV-2 but cannot eliminate the existing virus. Therefore, an RNA replication inhibitor requires a combination of immunity, thus, with an unavoidable immune inflammation.

A system involving numerous proteins and cells such as neutrophils, macrophages, killer T cells, and various cytokines has been established in the immune system of the living body to contribute to infection defense.[20–23] Neutrophils and macrophages, the center of the immune system, phagocytose foreign pathogenic viruses that have infiltrated the body and use of reactive oxygen species (ROS) to oxidize and decompose them. Thus, superoxide radical anion ($O_2^{\bullet-}$), the center of the ROS family in the terminal of the immune mechanism, is produced and oxidatively decomposes foreign substances such as viruses.[22] However, it is said that when excessively produced $O_2^{\bullet-}$ attack cells, it induces tissue inflammation. Therefore, immune oxidation must be used to break out the virus while also keeping it from multiplying, and an analog drug that acts under inflammatory conditions is required. In an inflamed organ, the degradation and inactivation of analog drugs due to the ROS redox reaction under the immune system are inevitable. Therefore, it is important to know the redox reaction between ROS and antiviral drugs in preventing its degradation and maximizing the concentration at the inflamed organ.

Several redox mechanisms between $O_2^{\bullet-}$ and acidic substrates such as T-705 are known, such as superoxide-facilitated oxidation (SFO),[24–26] hydrogen–atom transfer involving proton-coupled electron transfer (PCET),[27–31], and sequential proton-loss electron transfer.[32] In the SFO mechanism, the initial proton transfer (PT) from the substrate to $O_2^{\bullet-}$ to give a hydroperoxyl radical ($HO_2^{\bullet}$) is followed by rapid dismutation to give hydroperoxide (H_2O_2) and dioxygen (O_2). Then, the substrate anion is oxidized by the O_2 formed in the dismutation process.[33] Conversely, the other two mechanisms involve direct oxidation by $O_2^{\bullet-}$ or $HO_2^{\bullet}$. Considering the possible

mechanisms and structure–decomposability relationship of T-705, its T-1105 moiety is thought to play a significant role in the oxidative decomposition mechanism. Our previous studies reported that $O_2^{\bullet-}$ is eliminated by polyphenols,[30] 1,4- and 1,2-benzendiols (hydroquinone[29] and catechol[28]), and mono-phenols including aminophenols[31,34] through the oxidative electron transfer (ET) involved in the PCET. In these studies, the PCET mechanism is based on quinone–hydroquinone π-conjugation and involves two PTs and one ET.

In the present study, we have conducted a mechanistic analysis based on electrochemistry and theoretical calculations on the reactivity between T-705 (T-1105) and electro-generated $O_2^{\bullet-}$. Accordingly, we present valuable information regarding the degradation of pyrazine antiviral RNA-analog-drugs by $O_2^{\bullet-}$, which is assumed to be important to manage the concentrations of antiviral drugs in an inflamed organ. It is hoped that this study provides an insight into the antiviral drugs that are not easily metabolized, thereby expanding the point to consider drug design and utility, such as enhancement of net pharmacological activity and reduction of side effects associated with less dosage.

2 RESULTS & DISCUSSION

2.1 Reactivity between Electro-generated $O_2^{\bullet-}$ and Pyrazine Antiviral Drugs

2.1.1 Cyclic Voltammograms (CV) of $O_2/O_2^{\bullet-}$in the presence of Pyrazine Antiviral Drug

Based on electrochemical measurements in *N*, *N*-dimethylformamide (DMF), the reactivity between pyrazine antiviral drugs and $O_2^{\bullet-}$ was discussed (Supporting Information, Figure S1). Figure 1 shows the CVs for saturated O_2 (4.8×10^{-3} mol dm^{-3}) in the presence of T-1105 (a), T-705 (b) phenol (c), and catechol (d). The CVs obtained in the presence of phenol and catechol were reported in our previous paper,[28–31] and are presented here for comparison to show the CV behavior demonstrating an ET between $O_2^{\bullet-}$ and substrate. In aprotic and unbuffered solvents

such as DMF, O_2 shows quasi-reversible redox at −1.284 V vs ferrocenium ion/ferrocene (Fc^+/Fc) couple (Equation (1)), resulting in the formation of $O_2^{\bullet-}$ in the initial cathodic scan and reoxidation to O_2 in the returned anodic scan (solid lines, Figure 1a–d). The reversible CVs investigated here were all modified to irreversible CVs with a loss of anodic current by the presence of the protic compounds (a–d) in a concentration-dependent manner, suggesting that the initial homogeneous reaction between electro-generated $O_2^{\bullet-}$ and the compounds are PT. This result is supported by the fact that the CV traces in the absence of O_2 (removed by bubbled dinitrogen (N_2)) show no peaks over the potential range investigated (data not shown). Thus, the loss of reversibility in the $O_2/O_2^{\bullet-}$ is due to the PT from the compounds forming $HO_2^{\bullet}$ (Equation (2)).

In the presence of phenol (Figure 1c), the bioelectronic CV with an additional pre-peak on the cathodic scan was observed, which is driven by the exergonic reduction of the resulting $HO_2^{\bullet}$/hdroperoxyl anion (HO_2^-) after the primary electrode process associated with PT, leading to the irreversible overall reduction of O_2 to H_2O_2. Conversely, in the presence of pyrazine antiviral drugs (a, b), the CV traces do not show bioelectronic characteristics owing to the elimination of $HO_2^{\bullet}$ by those anions (T-1105$^-$, T-705$^-$) through the subsequent ET (Equation (4)) forming corresponding radicals (T-1105$^{\bullet}$, T-705$^{\bullet}$), similar to that in the presence of catechol (d). That is, Figure 1a–b demonstrates that T-1105 and T-705 was chemically oxidized by $O_2^{\bullet-}$, through the first PT and subsequent ET.

$O_2 + e- \leftrightarrow O_2^{\bullet-}$	$E° = -1.284$ V vs Fc^+/Fc	(1)
$O_2^{\bullet-} + \text{T-705} \rightarrow HO_2^{\bullet} + \text{T-705}^-$	the first PT	(2)
$HO_2^{\bullet} + e- \rightarrow HO_2^-$	$E° = -0.4$ to -0.2 V vs Fc^+/Fc	(3)
$HO_2^{\bullet} + \text{T-705}^- \rightarrow HO_2^- + \text{T-705}^{\bullet}$	ET	(4)
$HO_2^- + H^+ \rightarrow H_2O_2$		(5)

where $E°$ (V vs Fc^+/Fc) is the standard redox potential.

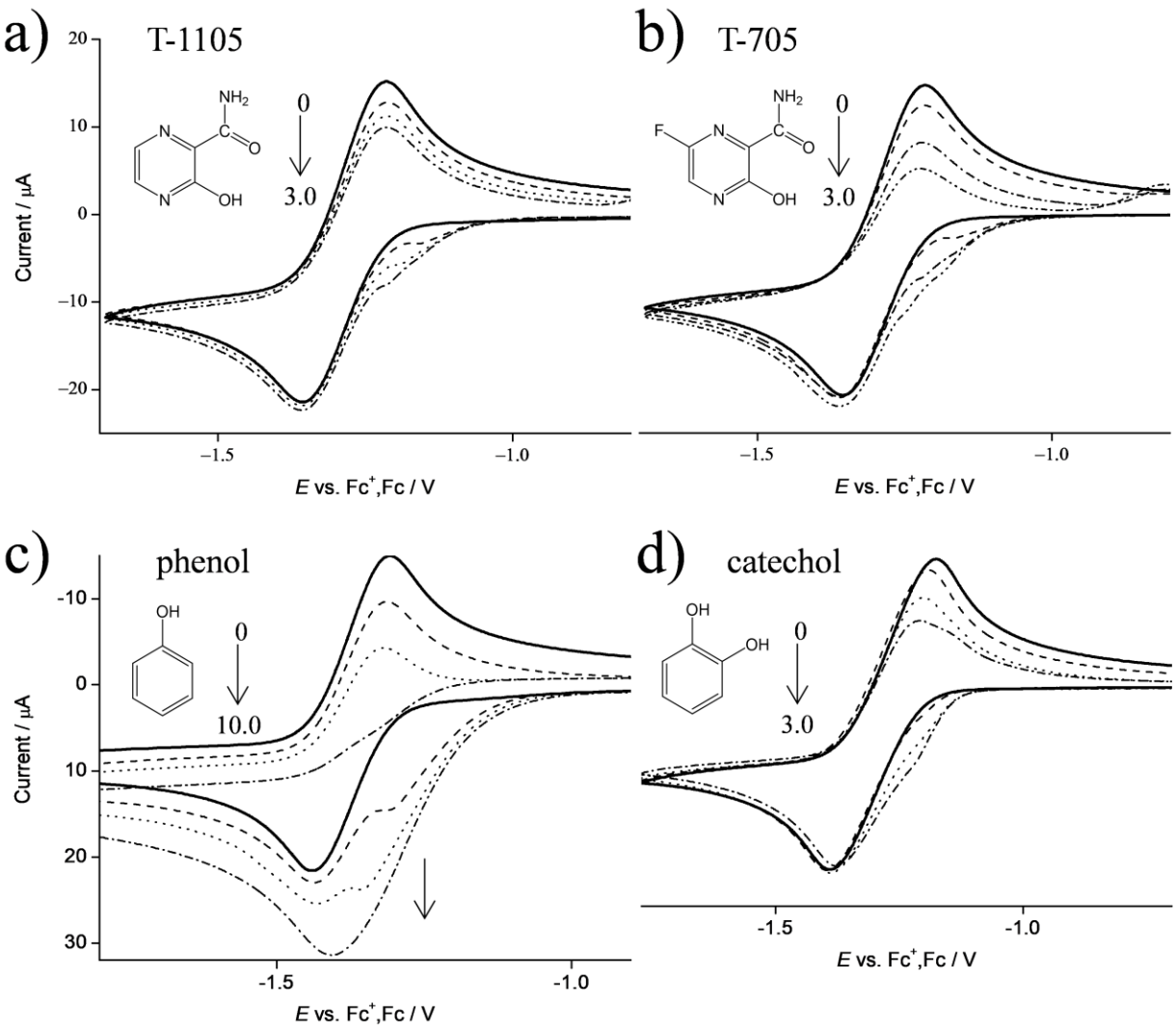

Figure 1. CVs of O_2 (4.8×10^{-3} mol dm^{-3}) in the presence of (a) T-1105, (b) T-705, (c) phenol, and (d) catechol, in DMF containing 0.1 mol dm^{-3} tetrapropylammonium perchlorate (TPAP), recorded with a glassy carbon (GC) electrode (Φ = 1.0 mm) at a scan rate of 0.1 V s^{-1}. Concentrations ($\times 10^{-3}$ mol dm^{-3}) are 0, 1.0, 2.0, 3.0 (a, b, and d), and 0, 3.0, 5.0, and 10.0, (c) (the concentration changes are shown by arrows).

2.1.2 *In Situ* Electrolytic Ultraviolet–visible (UV–Vis) Spectral Analysis of Reactivity between Pyrazine Antiviral Drugs and $O_2^{\bullet-}$

The reactivity between T-705 and electro-generated $O_2^{\bullet-}$ was confirmed, through *in situ* electrolytic UV–Vis spectral measurements using the optically transparent thin layer electrochemical (OTTLE) cell (Supporting Information, Figure S2). First, the electrochemical oxidation of T-705 at a GC electrode in a DMF solution under purging N_2 was conducted using cyclic voltammetry (Figure 2a). Over the accessible potential range (+1.5 to 0 V vs. Fc^+/Fc) in DMF, no peak was observed for the oxidation of T-705 but for the electrolysis of DMF solvent (E_{pa} = 1.2 V vs. Fc^+/Fc, shown by a circle). Next, Sodium methoxide (CH_3ONa) as a Brønsted base (an alkali agent) was added to the solution, and an anodic peak appeared at around 0.55 V in the CVs with the concentration dependency (the voltammetric behavior was the same for T-1105). Therefore, the observed anodic peak will derive from the oxidation of T-705$^-$ generated after deprotonation by CH_3ONa (Equation (6)). The observed CV was irreversible and broadened, implying that the deprotonated T-705$^-$ was irreversibly oxidized at more than one electron and chemically irreversible to a starting material. That is, the deprotonated T-705$^-$ is easily decomposed at the electrode surface through base-catalyzed oxidation. Though details of the electrochemical mechanism causing broaden peak are unclear, some oxidation mechanisms related to the acid-base reaction, i.e., sequential proton-electron transfer (PT–ET) and concerted PT–ET, are possible remains controversial.

$$\text{T-705} + CH_3ONa \rightarrow \text{T-705}^- + Na^+ + CH_3OH \quad (6)$$

Considering these CV results, *in situ* electrolytic UV–Vis spectra for the CV solution containing T-705 (1.0×10^{-3} mol dm^{-3}) were measured in the absence of O_2 under purging N_2 and in the presence of O_2 (b). The spectrum of T-705 alone has a characteristic absorption band centered at 282 nm. Under applied potential at +1.5 to –2.0 V vs. Fc^+/Fc without O_2, the spectrum did not change where any potential was applied (data in not shown), demonstrating that

T-705 is not electrolyzed without deprotonation, which is in reasonable agreement with CV results shown in Figures 2a. Conversely, the spectrum has changed in the presence of CH_3ONa (5.0×10^{-3} mol dm^{-3}) without applying a potential (red line). Since T-705 is deprotonated by CH_3ONa as a Brønsted base, the spectrum centered at 313 nm will be attributed to T-705^{-}, showing the red-shift of spectrum peak.

On the other side, spectral of T-705 in the presence of saturated O_2 (4.8×10^{-3} mol dm^{-3}) has changed, decreasing the intensity at applied cathodic potentials over −1.2 V corresponding electrogeneration of $O_2^{\bullet-}$ (Figure 2c). Furthermore, being kept the potential at −1.6 V for 10 min, the spectrum of T-705 disappeared. These spectral changes have demonstrated that product of homogeneous reaction between T-705 and $O_2^{\bullet-}$ is not T-705^{-}. By analogy with the CV results, the initial PT (Equation (2)) and the following reactions including ET between $HO_2^{\bullet}$ and T-705^{-} (Equation (4)) rapidly undergo base-catalyzed oxidation, resulting degradation of T-705/T-705^{-}. Measured in the OTTLE cell having a 1.0–mm thin layer, the spectra immediately disappeared when the potential was applied. Thus, the following reactions will proceed in a superior kinetics via the intermediates; T-705^{-} and T-$705^{\bullet}$, otherwise concertedly with the initial PT. Since the radical product was undetectable using *in situ* electrolytic electron spin resonance (ESR) system (Supporting Information, Figure S2), T-$705^{\bullet}$ would be decomposed at the subsequent reaction (no data is shown). These series of reactions, the initial PT (Equation (2)) followed by the subsequent oxidation and others, are referred to as the base-catalyzed oxidation process or the SFO.[24,25] The SFO is the oxidation of the substrate anion (generated by alkali $O_2^{\bullet-}$) by O_2. When considering the superior kinetic expected from the CV and *in situ* spectral results, the mechanism will involve the sequential ET from T-705^{-} to $HO_2^{\bullet}$ coupled to the initial PT; i.e., PCET, rather than SFO.

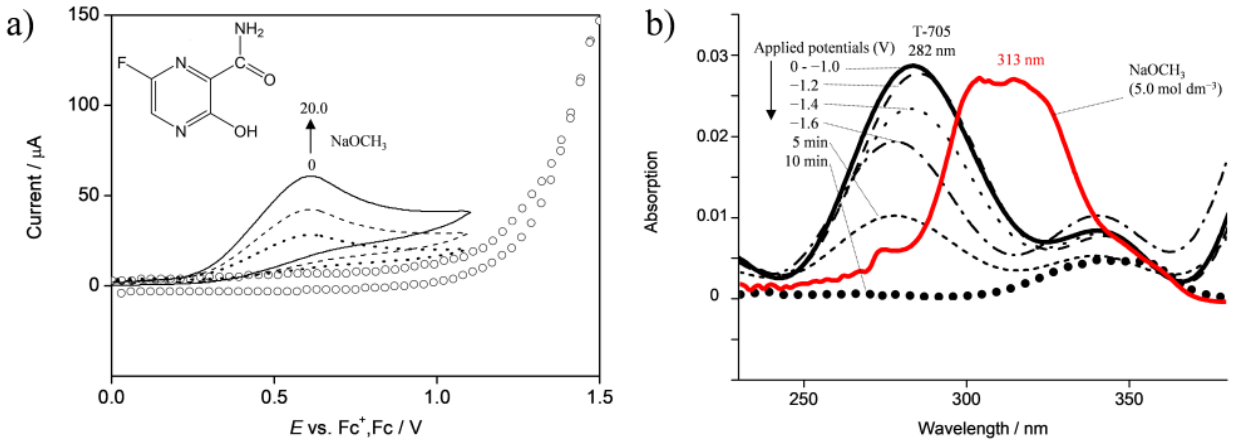

Figure 2. (a) CVs of T-705 (10.0×10^{-3} mol dm^{-3}) in the absence (circle) and in the presence of CH_3ONa (0, 5.0, 10.0, and 20.0×10^{-3} mol dm^{-3}) in DMF containing 0.1 mol dm^{-3} TPAP recorded with a GC electrode (Φ = 1.0 mm) at a scan rate of 0.1 V/s. (b) UV–Vis spectral changes of T-705 (1.0×10^{-3} mol dm^{-3}) solutions in the absence (black bold) and presence (red bold) of CH_3ONa (5.0×10^{-3} mol dm^{-3}), and *in situ* electrolytic UV–Vis spectra of T-705 in the presence of saturated O_2. The controlled-potential at −1.0, −1.2, −1.4, and −1.6 V vs. Fc^+/Fc was applied to the solutions.

As shown above, the CV traces for $O_2/O_2^{\bullet-}$ in the presence of the compounds are divided into two typical curves: type A, an irreversible one electron process (Equations (1), (2), and (4)) leading to $O_2^{\bullet-}$ elimination, which is typically observed with the catechol moiety as reported in our previous paper. And type B, an irreversible two-electron process observed in electro–chemical–electro (ECE) reactions (Equations (1)–(3)). In this scenario, Figure 3 shows the plausible electrochemical mechanisms for $O_2/O_2^{\bullet-}$ in the presence of (a) T-705 (type A) and (b) phenol (type B), summarizing Equations (1)–(5). Furthermore, type A involves efficient PT–ET between T-705 and $O_2^{\bullet-}$ through the PCET mechanism resulting degradation of T-705.

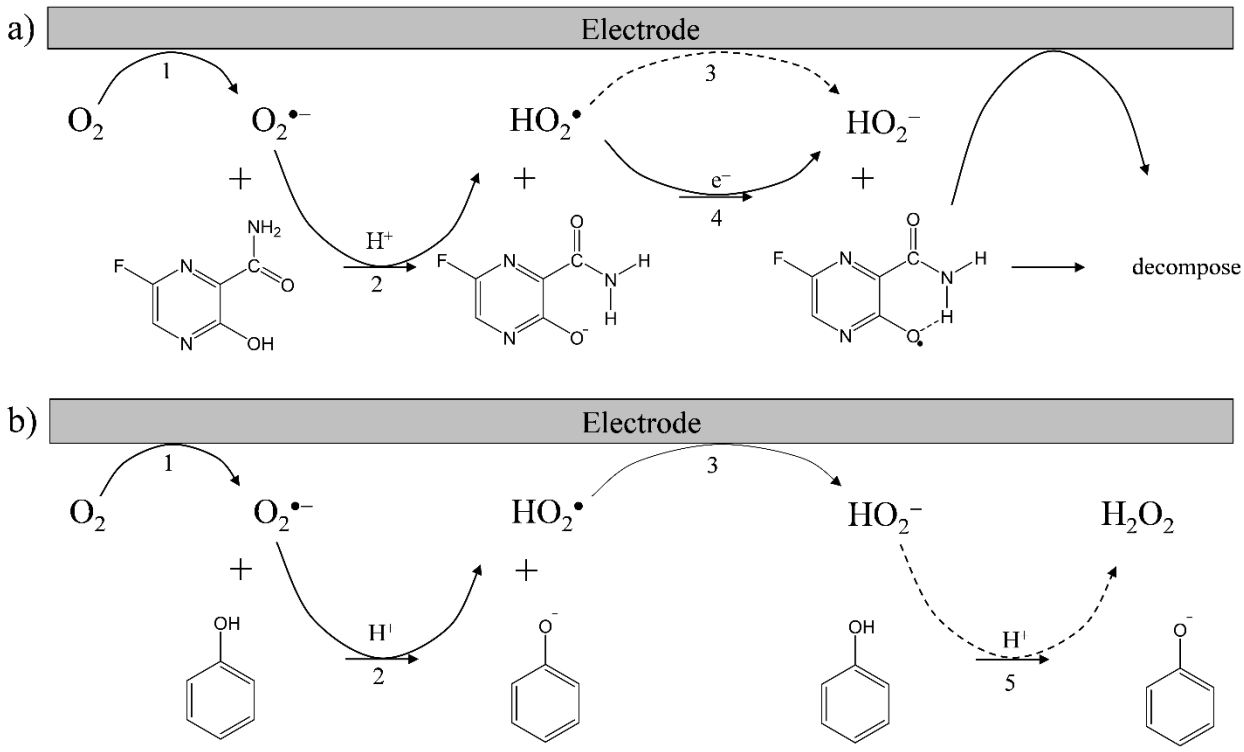

Figure 3. Plausible electrochemical mechanism for $O_2/O_2^{\bullet-}$ in the presence of (a) T-705 and (b) phenol in DMF. [1]One-electron reduction of $O_2/O_2^{\bullet-}$; [2]the first PT from the acidic substrate to $O_2^{\bullet-}$; [3]one-electron reduction of $HO_2^{\bullet}/HO_2^-$; [4]ET from substrate anion to $HO_2^{\bullet}$; [5]the second PT to HO_2^-.

2.2 Density Functional Theory (DFT) Analyses of the PCET Reaction between Pyrazine Antiviral Drugs and $O_2^{\bullet-}$

2.2.1 Optimization of Stable Structures of T-705 and Its Corresponding Chemical Species along the PCET

DFT calculations were performed with the Becke three-parameterLee‐Yang‐Parr (B3LYP) hybrid functional employing the polarized continuum model (PCM) method to aid the mechanistic analysis of the PCET between pyrazine antiviral drugs (T-1105, T-705) and $O_2^{\bullet-}$ in DMF. First, to obtain the structures of the stable conformer of T-705 and its corresponding

chemical species along the PCET, energy scanning for the dihedral angle around the 2-carboxamide group was performed. Figure 4 shows the optimized structures of two T-705-conformers (T-705^{a}, T-705^{b}), the T-705^{-} upon initial PT (−H^{a1}, −H^{a2}, −H^{b}), and the T-705$^{\bullet}$ after the subsequent ET (−H^{a}–e, –H^{b}–e). Calculated standard Gibbs free energy changes ($\Delta G°$ / kJ mol^{-1}, 298.15 K) for the chemical species, and bond length (Å) of intramolecular hydrogen bonds (HB) are denoted.

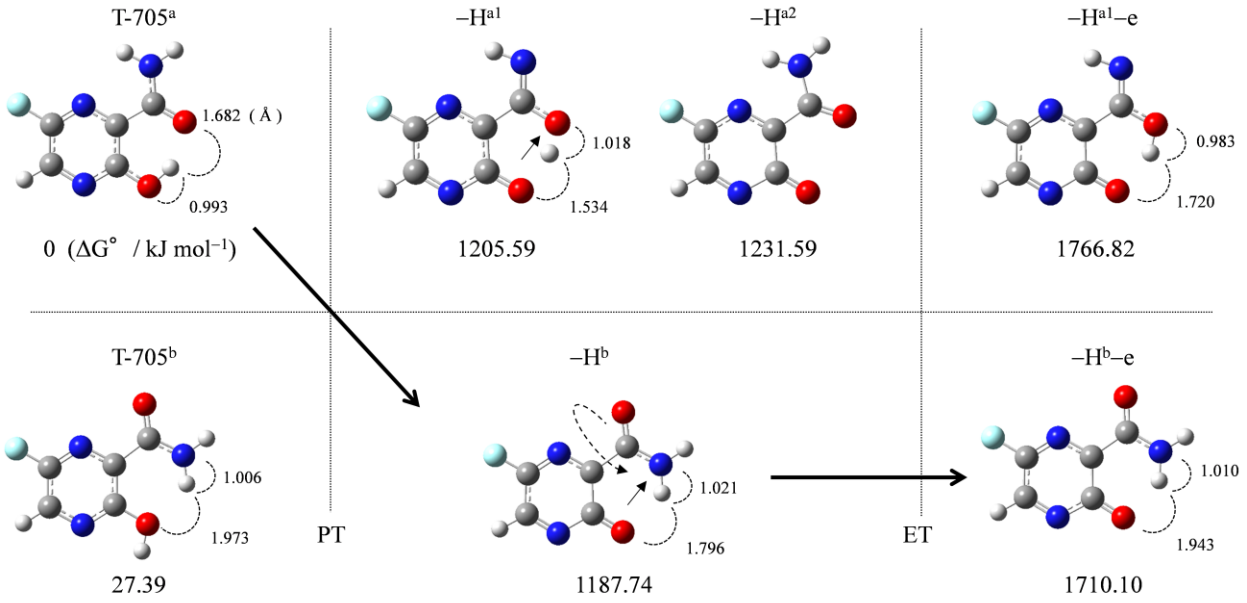

Figure 4. Different conformers of T-705 (T-705^{a}, T-705^{b}), T-705^{-} (−H^{a1}, −H^{a2}, −H^{b}), and T-705$^{\bullet}$ (−H^{a1}−e, −H^{b}−e) along the PCET reaction calculated DFT-B3LYP/PCM/6-311+G(3df,2p) in DMF, denoted with calculated $\Delta G°$s for each chemical species (kJ mol^{-1}, 298.15 K) and bond length of intramolecular HBs (Å).

T-705 has two planar conformers (T-705^{a} and T-705^{b}) that differ in the orientation of the dihedral angle around the 2-carboxamide group, forming an intramolecular HB between the adjacent 3-hydroxyl group. Comparison of the $\Delta G°$s shows that T-705^{a} is more stable than T-705^{b} by 27.39 kJ mol^{-1}. Therefore, the 2-carboxamide-proton of T-705^{a} will be deprotonated

upon the initial PT because the 3-hydroxyl-proton is forming HB. However, the stable conformers for both of the T-705^{-} and T-705$^{\bullet}$ were T-705^{b} derivatives; –H^{b} (1187.74), and –H^{b}–e (1710.10), respectively. Thus, these calculation results imply that the 2-carboxamide group rotates along the initial PT process of the PCET. Furthermore, 3-hydroxyl-proton will be gravitated toward the 2-carboxamide side after its rotation forming –H^{b} (bond lengths (Å), N–HO: 1.021, NH–O: 1.796). In this way, the initial PT forming –H^{b} occurs accompanied by the dihedral rotation of the 2-carboxamide group and the reformation of intramolecular HB for its stabilization.[35]

2.2.2 Change in HOMO–LUMO Energies upon PCET between T-705 and $O_2^{\bullet-}$

Figure 5 shows HOMO–LUMO energy change along the PCET between T-705 and $O_2^{\bullet-}$, calculated by the DFT method. After the initial PT, some reactant species (conformers), i.e., T-705^{a}, T-705^{b}, the T-705^{-} (–H^{a1}, –H^{a2}, –H^{b}), $O_2^{\bullet-}$, and $HO_2^{\bullet}$ coexist in the solution. The SOMO energy (Hartree) for $HO_2^{\bullet}$ (−0.3142) is much lower than HOMO energies for T-705 and T-705^{-}. Thus, the electron acceptor will be $HO_2^{\bullet}$, not $O_2^{\bullet-}$. Considering the CV results in Figure 1 that the generated $HO_2^{\bullet}$ is not detected at the electrode reaction with the energy scanning shown in Figure 4, the electron donor will be –H^{b} formed after the initial PT with dihedral rotation, for which the bold red line indicates the downhill energy relationship in Figure 5. Thus, this change in HOMO–LUMO energies upon PT between the T-705 and $O_2^{\bullet-}$ forming –H^{b} and $HO_2^{\bullet}$ and the subsequent ET is reasonable for the fact that $HO_2^{\bullet}$ was eliminated in the CV.

The HOMO–LUMO relationship between the products after ET (i.e., –H^{b}–e and HO_2^{-}) is reversed, which is rational for orbital energies in reverse ET (red dotted line in Figure 5). However, the HOMO (−0.2754) of the PT-forming H_2O_2 is lower than the HOMO (−0.1648) of HO_2^{-}, making the reverse ET impossible. Thus, the second PT is dominant in determining the ET

direction. Notably, only one conformer (–2H^{b}–e) formed after the dihedral rotation of the 2-carboxamide group was adaptable for the radical cation due to the stability of intramolecular HB.

As a result, the HOMO–LUMO relationship analysis suggests that the plausible PCET mechanism involves two PTs and one ET with essential dihedral rotation for successful ET eliminating $HO_2^{\bullet}$ with good agreement with the electrochemical results.

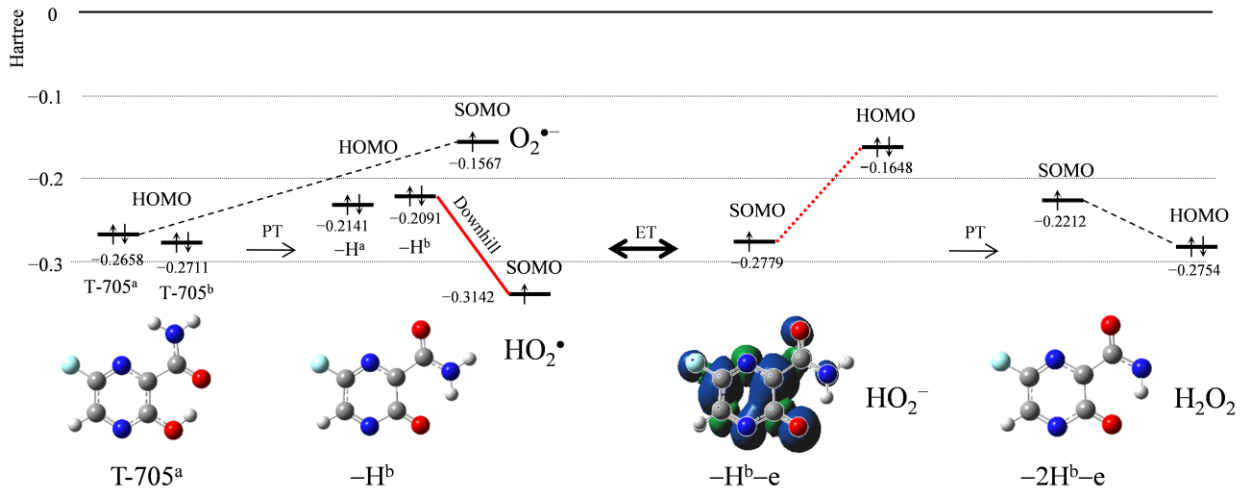

Figure 5. Change in HOMO–LUMO energies (Hartree) upon PCET between $O_2^{\bullet-}$ and two conformers of T-705 (T-705^{a}, T-705^{b}) with their corresponding chemical species in DMF, calculated with the DFT-B3LYP/PCM/6-311+G(3df,2p).

2.2.3 Free Energy Analysis of PCET between T-705 and $O_2^{\bullet-}$.

In Figure 6, an equilibrium scheme and ΔG° values for the six diabatic electronic states in the PCET between T-705 and $O_2^{\bullet-}$ as calculated using DFT are shown. The important factors in determining the sequential processes shown in this scheme are the ΔG°s for the acid-base interaction and the redox potentials of the components. ET1 is strongly endergonic (ΔG° = 474.5 kJ mol^{-1}); thus, PT1 (3.1) coupled with the rotation of the dihedral angle around the 2-carboxamide group forming −H^{b} will first occur as suggested in the *in situ* electrolytic UV–Vis

spectral results shown in Figure 2. In the following pathways, both PT3 (398.9) and ET2 (122.6) are endergonic, suggesting that the sequential PCET does not proceed contrary to the electrochemical results. However, the ET2 is promoted by the following PT4 (−14.0); the second PT. As shown in the HOMO–LUMO relationship (Figure 5), the second PT is necessary for successful ET along the PCET. Thus, the proton and electron is transferred in one kinetic process corresponding to the diagonal of the rectangle in Figure 5, labeled concerted PCET (108.5), rather than a sequential pathway of ET2–PT4.

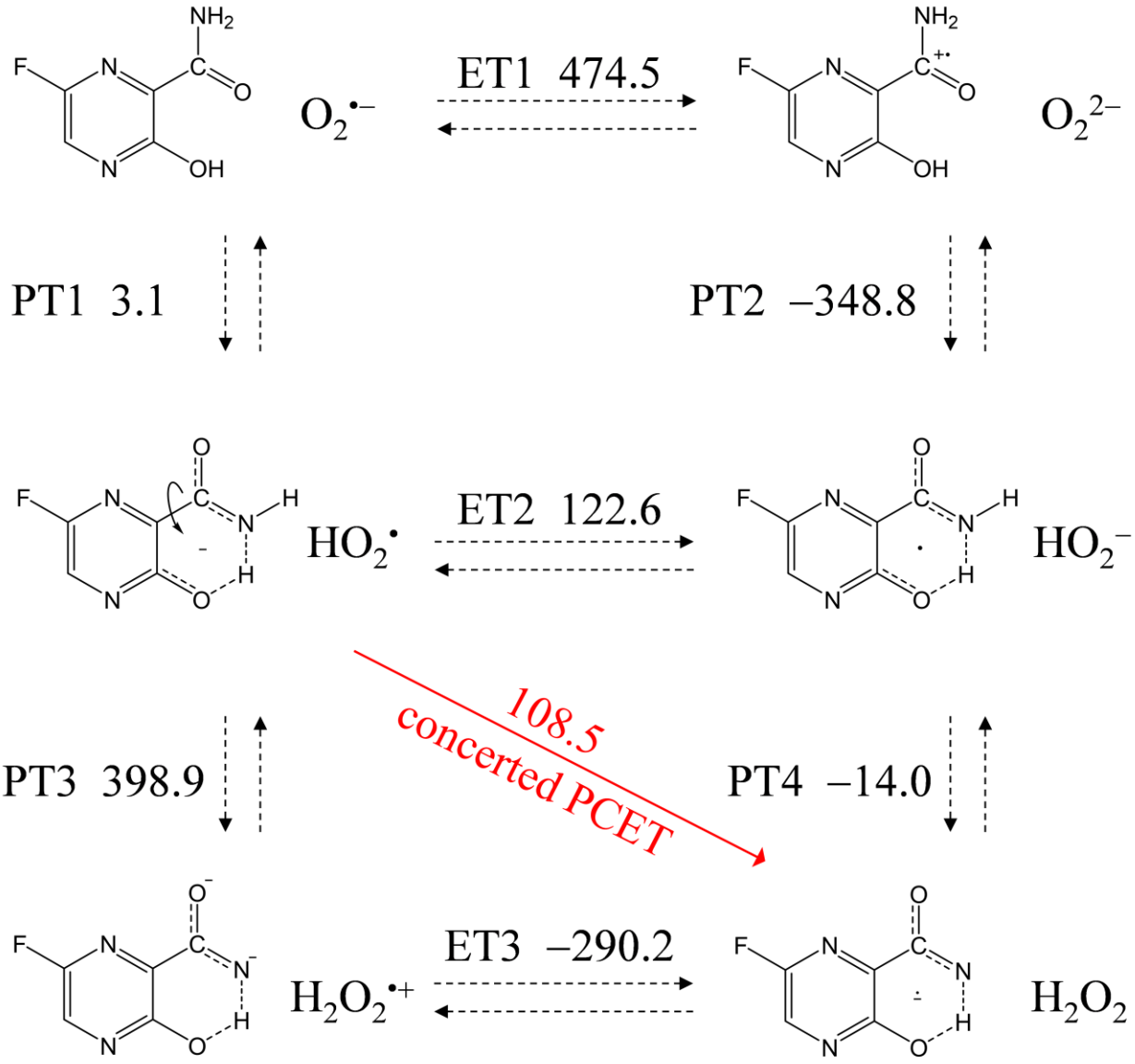

Figure 6. Six diabatic electronic states and the $\Delta G°$s values for the PCET between T-705 and $O_2^{\bullet-}$ involving two PTs and one ET in DMF. $\Delta G°$s (kJ mol^{-1}, 298.15 K) for PT (PT1–PT4), ET (ET1–ET3), and concerted PCET were calculated using the DFT-(U)B3LYP/PCM/6-311+G(3df,2p) method.

2.2.4 Potential Energy Surfaces of the PCET between T-705 and $O_2^{\bullet-}$

To clarify the oxidative degradation through the PCET mechanism, potential energy surfaces were investigated. After the initial PT forming T-705^- and $HO_2^\bullet$ as free reactants (FR), it is assumed that the reaction involves three elementary steps: i) formation of the pre-reactive complex (PRC) from the FR, ii) reaction to the product complex (PC) via a transition state (TS), and iii) dissociation of the PC yielding free products. Furthermore, the structural and electronic changes during the reaction were analyzed with the natural bond orbital (NBO) calculations at the DFT-(U)B3LYP/PCM/6-311+G(3df,2p) level of theory in DMF. We started with an analysis of potential energy scanning for the stable PRC (T-705^-—$HO_2^\bullet$) and PC (−2H−e—H_2O_2), then optimized structures of plausible PRC and PC with the TS were obtained. In Figure 7, (a) energy profiles ($\Delta G°$, kJ mol^{-1}), and (b) changes in N-H and H-O bond distances with the number of electrons on π-orbital of T-705, along the IRC for the PCET involving one ET and one PT forming the PC are shown. The IRC shows that a concerted PCET occurs between T-705^- and $HO_2^\bullet$ in one kinetic process via the TS of low activation energy (E_a) at 64.65 kJ mol^{-1} without generating any intermediates.

Then, spin density distributions localizing the atoms consisting of the radical before and after the TS along the PCET are demonstrated in Figure 7(b), showing that the radical localized on $HO_2^\bullet$ in the initial system was transferred to T-705^- in the resulting reaction system. Changes in the spins on the electron donor side (T-705^-) and acceptor side ($HO_2^\bullet$) are in good correlation

with the changes of π-electron of T-705^{-} side. These results show that the π-electron of T-705 is transferred concertedly with the second PT.

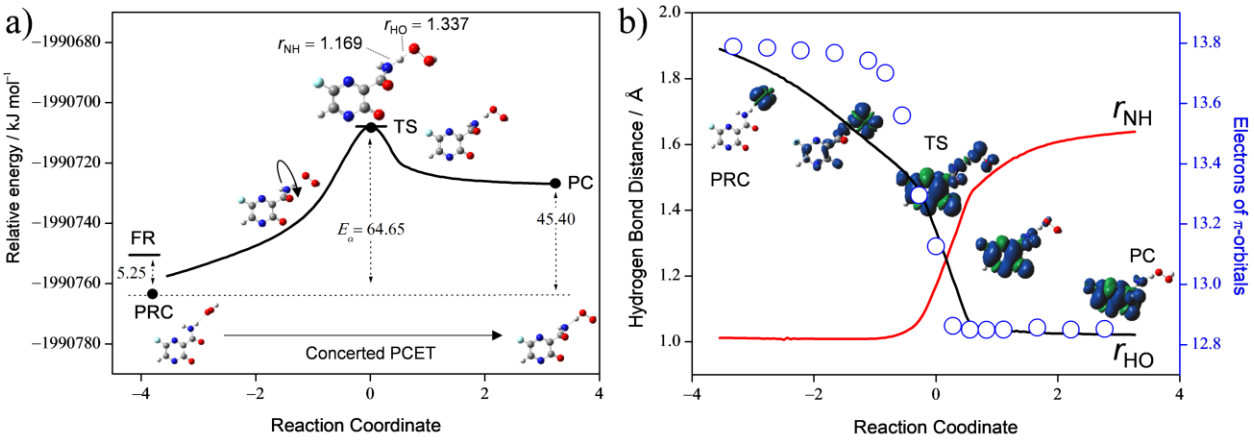

Figure 7. (a) IRC of the concerted PCET between T-705^{-} and $HO_2^{\bullet}$, and structures along with the IRC, PRC (T-705^{-}—$HO_2^{\bullet}$), TS with HB lengths (Å, r_{NH} and r_{HO}), and PC. (b) Changes in N–H bond (r_{NH}, red line) and H–O (r_{HO}, black line) bond lengths (Å, corresponding to the labels of the left vertical axes), and the number of electrons (open circles) on the π-orbitals in the T-705 moiety (corresponding to the labels of the right vertical axes). The calculations were performed using the DFT-(U)B3LYP/PCM/6-311+G(3df,2p) method. The NBO analyses obtained π-electrons and spin density distributions localizing the atoms constituting the radical before and after the PCET and at the TS shown in (b).

For a comparative study, the $\Delta G°$ and the E_a of T-1105 and catechol along the PCET were also calculated (Table 1). The $\Delta G°$s for the concerted PCET between $HO_2^{\bullet}$ and deprotonated anion, formed after the PT1, were obtained from the sum of the values for ET2 and PT4 (or for ET3 and PT3), respectively. Then, the total values of $\Delta G°$s for the net PCET were obtained from the values for the two PTs and one ET. From a thermodynamic viewpoint, the total values cannot embody the energetic driving force of the net PCET for the T-1105 (117.4) and T-705 (111.7) because the $\Delta G°$s for the unfeasible ET process has been summed in those. Conversely, the total

value for the catechol (−394.3) embodies the energetic driving force, as shown in the CV (Figure 1(d)). Thus, the important factor for the net PCET pathway comprised PT1–ET2–PT4 to proceed as a sequential reaction is the Δ*G*°s for the individual reactions, rather than the total Δ*G*°s. Notably, both the total Δ*G*° and the Δ*G*°s of individual reactions along the plausible pathway, the sequential PCET comprised PT1–ET2–PT4 or the PT1–concerted PCET, indicate that the net PCET between T-705 (T-1105) and $O_2^{\bullet-}$ is unfeasible. Therefore, thermodynamic analyses did not clarify whether the PCET between T-705 (T-1105) and $O_2^{\bullet-}$ proceeds via a concerted or sequential pathway. However, the fact that the Δ*G*° result was opposite to the electrochemical result (Figure 1) implies that the kinetic insights into the degradation of T-705 (T-1105) through the PCET are needed.

Table 1. Δ*G*º Values (kJ mol^{-1}, 298.15 K) of Six Diabatic Electronic States for PCET between $O_2^{\bullet-}$ and the Three Compounds (T-1105, T-705, and catechol) in DMF, Calculated Using DFT at the B3LYP/PCM/6-311+G(3df,2p) Level.

Compounds	Δ*G*° / kJ mol^{-1}									^4E_a /kJ mol^{-1}
	[1]PT1	PT2	PT3	PT4	ET1	ET2	ET3	[2]Concerted	[3]Total	
T-1105	8.2	−337.1	407.5	−20.6	475.2	129.8	−298.3	109.2	117.4	68.82
T-705	3.1	−348.8	398.8	−14.0	474.5	122.6	−290.2	108.5	111.7	64.65
catechol	−296.1	−336.7	365.1	−97.7	40.1	−0.4	−463.3	−98.2	−394.3	52.50

[1]Each reaction process, PT1-PT4 and ET1-ET3. [2]Concerted values involve the sum of Δ*G*°s for ET2–PT4 (PT3–ET3). [3]Total values involve the sum of Δ*G*°s for two PTs and one ET. ^4E_a values of concerted PCET for T-1105 and T-705 and concerted 2PCET for catechol

The obtained E_a values are feasible for the concerted PCET, with a good correlation with the CV results. The notable finding was that the E_a value for T-705 (64.65) is close to that for catechol (52.50), whose kinetics are superior due to the concerted 2PCET pathway.[28] Careful

observations of the changes in structures in the reaction coordinate (Figure 7(b)) indicate that the concerted PCET occurs simultaneously with the deheadral rotation of the 2-carboxiamide group, implying that the rotation enables superior kinetics of the concerted PCET.

To clarify the oxidative degradation mechanism of the pyrazine antiviral drugs by $O_2^{\bullet-}$ through the thermodynamically unfeasible PCET, it is assumed that i) the PCET proceeds thorough the concerted manner with superior kinetics apart from the thermodynamic energetics of the chemical species, ii) the radical product of the PCET ($-2H^b-e$) irreversibly and quickly decomposes. Regarding ii) the degradation of $-2H^b-e$, the electrochemical and calculation analyses do not clarify its mechanism; however, since the radical product unambiguously is undetectable using *in situ* electrolytic UV–Vis and ESR system, $-2H^b-e$ would quickly be decomposed. Thus, since the irreversible degradation of $-2H^b-e$ occurs following the PCET, the square equilibrium of the PCET shown in Figure 6 will be promoted by the subsequent degradation.

In Figure 8, the net mechanism of the oxidative degradation of T-705 by $O_2^{\bullet-}$, thorough the initial PT and subsequent concerted PCET along the rotation of the dihedral angle around the 2-carboxamide group is shown. It is presumed that the high reactivity of T-705 and T-1105 with $O_2^{\bullet-}$, similar to that for catechol, is due to the mechanism. The PCET involving two PTs and one ET between catechol and $O_2^{\bullet-}$ based on quinone–hydroquinone π-conjugation form quinone radical anion as a product.[28] However, quinone radical anion is moderately stable in aprotic solution, at least on the CV time-scale and *in situ* ESR time-scale; thus, the subsequent degradation is less associated with kinetics of the net PCET. That is, the degradation of $-2H^b-e$ promotes the net PCET between T-705 and $O_2^{\bullet-}$ demonstrating the catechol-like reactivity in the CV.

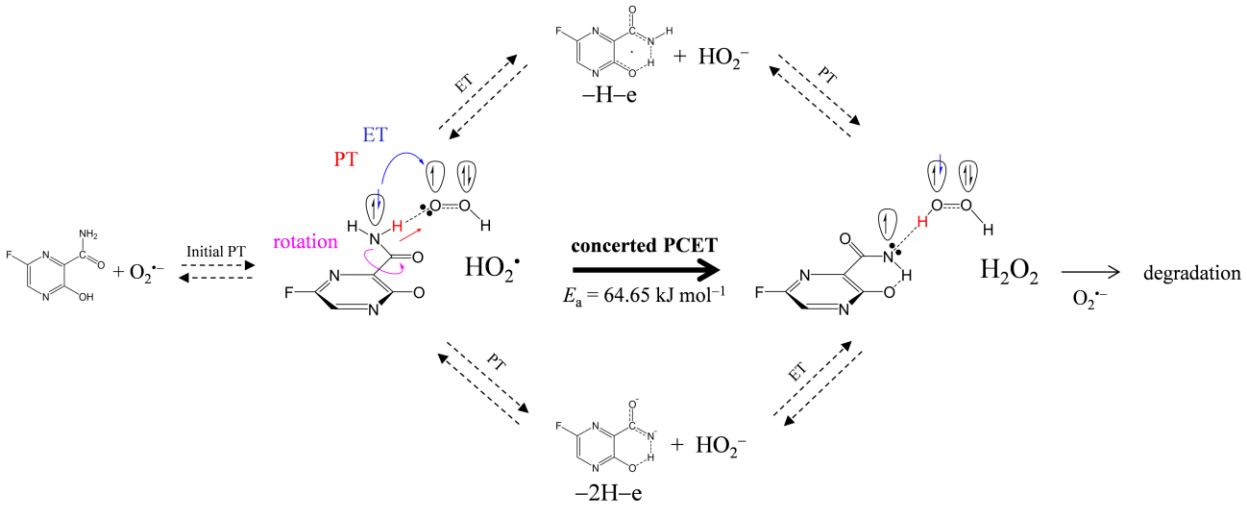

Figure 8. Mechanism of the oxidative degradation of T-705 by $O_2^{\bullet-}$ thorough the initial PT followed by concerted PCET with rotation of the dihedral angle around the 2-carboxamide group.

3 CONCLUSION

In conclusion, we have investigated the reaction between electro-generated $O_2^{\bullet-}$ and pyrazine antiviral drugs in DMF. As a result, we have concluded that

- pyrazine antiviral drugs are easily decomposed by $O_2^{\bullet-}$ through the PCET involving two PTs and one ET;
- the concerted PCET after the initial PT occurs in one kinetic process via a TS without forming a high energy intermediate;
- the net reaction involves rotation of the dihedral angle around the 2-carboxamide group along the PCET;

The dihedral rotation of the 2-carboxamide group is necessary for successful PCET; then, the concerted PCET is the key process for the oxidative degradation of the pyrazine antiviral drugs by $O_2^{\bullet-}$. Therefore, if we can design a new pyrazine drug that inhibits the rotation of the dihedral angle around the 2-carboxamide group along the PCET, it may be possible to develop hypo-degradable antiviral drugs resistant to $O_2^{\bullet-}$.

Although the results presented in this manuscript are for a chemical reaction in an aprotic DMF solvent rather than a biological system, the PCET theory is adaptable to biological processes involving both protic and aprotic conditions in such as a lipid bilayer. Therefore, we hope that the findings obtained in this study will show a mechanism for the biological degradation of pyrazine antiviral drugs by $O_2^{\bullet-}$ in the living body.

4 MATERIALS & METHODS

4.1 Chemicals

T-1105, phenol, and catechol were purchased at best available grade (>99.8%) from Tokyo Chemical Industry Co., Ltd. (Tokyo, Japan) and used as received. T-705 was purchased at best available grade (>98.0%) from FUJIFILM Wako Pure Chemical Co., Ltd. (Osaka, Japan) and used as received. HPLC-grade anhydrous DMF, and CH_3ONa (95% powder) used in electrochemical and spectrum measurements were purchased from Sigma–Aldrich Inc (Tokyo, Japan) and were used as received. TPAP (>98.0%, Tokyo Chemical Industry Co., Ltd.) was purchased and recrystallized many times from ethyl methanol, then dried overnight at 313.15 K (40.0 °C) under reduced pressure, and dried again for 2 h or more immediately before use. Further details are given in a previous paper.[36,37] Ferrocene (Fc), used as a potential reference compound, was obtained from Nacalai Tesque Inc. (Kyoto, Japan) and purified by repeated sublimation under reduced pressure immediately before use.

4.2 Electrochemical and Electrolytic UV–Vis Spectral Measurements

Cyclic voltammetry was measured via a standard three-electrode system comprising a 1.0–mm diameter GC working electrode, a coiled platinum counter electrode, and an $Ag/AgNO_3$ reference electrode (containing acetonitrile solution of 0.1 mol dm^{-3} tetrabutylammonium perchlorate and 0.01 mol dm^{-3} $AgNO_3$; BAS RE–5) at 298.15 K (25.0 °C) using an ECstat-301

electrochemical analyzer coupled to electrochemical software (EC-frontier Co., Ltd.). The working electrode was polished with alumina paste on a polishing wheel before all experiments. The electrode was then rinsed with deionized water and acetone. After air drying, the electrode was ready to use. The reference electrode was calibrated with reference to the Fc^{+}/Fc couple, and all potentials reported here are referenced to the potential of this couple (Supporting Information, CV parameter).[28,30,35]

In situ electrolytic UV–Vis spectra were recorded using an OCEAN HDX spectrometer (OptoSirius Co., Ltd.). The controlled-potential electrolysis was performed at room temperature in an OTTLE cell (path length: 1.0 mm) using a Pt mesh working electrode (Supporting Information, Figure S2). A coiled platinum counter electrode and an $Ag/AgNO_3$ reference electrode was also used in the UV–Vis spectral measurements, as with the cyclic voltammetry measurements.[29]

To prevent contamination by moisture, samples were prepared in a glove box completely filled with N_2 gas. For the electro generation of $O_2^{\bullet-}$, a DMF solution containing 0.1 mol dm^{-3} TPAP as a supporting electrolyte was saturated with O_2 by air-bubbling the gas for ca. 2−3 min, and the gas was passed over the solutions during the electrochemical and electrolytic spectrometric measurements to maintain the concentration of O_2 at a constant level. The equilibrium concentration of O_2 was calculated as 4.8×10^{-3} mol dm^{-3}.

4.2.3 Theoretical Calculations

All calculations were performed at the DFT level with the B3LYP hybrid functional, as implemented in the *Gaussian 16* Program.[38] The geometry optimization, subsequent vibrational frequency calculations, and population analysis of each compound was performed by employing the standard split–valence triple ζ basis sets augmented by polarization 3df,2p and diffusion

orbitals 6–311+G(3df,2p). The solvent contributions of DMF, dimethylsulfoxide, acetonitrile, and water (Supporting Information, Table S1-S4) to the standard Gibbs free energies were computed employing the PCM method at the default settings of *Gaussian 16*, which is widely employed in the description of the thermodynamic characteristics of solvation. The zero-point energies and thermal correction, with entropy, were used to convert the internal energies to standard Gibbs energy at 298.15 K. The NBO technique was used for electron and spin calculations the population analyses.[39]

ASSOCIATED CONTENT

Supporting Information

The Supporting Information is available free of charge at DOI: (PDF)

Figure S1, CVs of $O_2/O_2^{\bullet-}$ in the presence of acidic substrate; CV parameters; Figure S2, *in situ* Electrolytic UV–Vis (OTTLE) and ESR spectral system; Figure S3, conformers of T-1105 with ΔGs; Table S1-S4, comparison of ΔGs for the PCET in dimethyl sulfoxide, acetonitrile, water, and vacuum; Table S5-S6, charge distribution and natural population on the TS structures; Table S7-S8, Calculated geometries of TS.

AUTHOR INFORMATION

Corresponding Author

Tatsushi Nakayama, Gifu Pharmaceutical University; 1-25-4 Daigaku–nishi, Gifu, 501-1196, Japan. Phone: +81-58-230-8100. Fax: +81-58-230-8200. E-mail: tnakayama@gifu-pu.ac.jp.

Author

Ryo Honda, United Graduate School of Drug Discovery and Medical Information Sciences, Gifu University; 1-1 Yanagido, Gifu, 501-1193, Japan.

Author Contributions

All authors contributed equally.

Funding Sources

This research did not receive any specific grant from funding agencies in the public, commercial, or not-for-profit sectors.

Notes

The authors declare no competing financial interest.

ACKNOWLEDGMENTS

The authors would like to thank Mr. Sugawara for his experimental assistance.

ABBREVIATIONS

PCET, proton–couple electron transfer; RdRp, RNA-dependent RNA polymerase; ROS, reactive oxygen species; SFO, superoxide-facilitated oxidation; PT, proton transfer; ET, electron transfer; CV, cyclic voltammogram; GC, glassy carbon; OTTLE, optically transparent thin layer electrochemical; ESR, electron spin resonance; DFT, density functional theory; B3LYP, Becke three-parameter Lee–Yang–Parr; PCM, polarized continuum model; HB, hydrogen bond; FR, free reactant; PRC, pre-reactive complex; PC, product complex; TS, transition state; NBO, natural bond orbital

REFERENCES

(1) Wang, X.; Xia, S.; Wang, Q.; Xu, W.; Li, W.; Lu, L.; Jiang, S. Broad-Spectrum Coronavirus Fusion Inhibitors to Combat COVID-19 and Other Emerging Coronavirus Diseases. *Int. J. Mol. Sci.* **2020**, *21*, 3843.

(2) Singh, A. A. K.; Singh, A. A. K.; Singh, R.; Misra, A. Remdesivir in COVID-19: A Critical Review of Pharmacology, Pre-Clinical and Clinical Studies. *Diabetes Metab. Syndr. Clin. Res. Rev.* **2020**, *14*, 641-648.

(3) Malin, J. J.; Suárez, I.; Priesner, V.; Fätkenheuer, G.; Rybniker, J. Remdesivir against COVID-19 and Other Viral Diseases. *Clin. Microbiol. Rev.* **2021**, *34*, 1-21.

(4) Khalili, J. S.; Zhu, H.; Mak, N. S. A.; Yan, Y.; Zhu, Y. Novel Coronavirus Treatment with Ribavirin: Groundwork for an Evaluation Concerning COVID-19. *J. Med. Virol*. **2020**, pp 740-746.

(5) Hutson, C. L.; Kondas, A. V.; Mauldin, M. R.; Doty, J. B.; Grossi, I. M.; Morgan, C. N.; Ostergaard, S. D.; Hughes, C. M.; Nakazawa, Y.; Kling, C.; Martin, B. E.; Ellison, J. A.; Carroll, D. D.; Gallardo-Romero, N. F.; Olson, V. A. Pharmacokinetics and Efficacy of a Potential Smallpox Therapeutic, Brincidofovir, in a Lethal Monkeypox Virus Animal Model. *mSphere.* **2021**, *6*.

(6) Li, D. D.; Han, R. M.; Liang, R.; Chen, C. H.; Lai, W.; Zhang, J. P.; H. Skibsted, L. Hydroxyl Radical Reaction with Trans-Resveratrol: Initial Carbon Radical Adduct Formation Followed by Rearrangement to Phenoxyl Radical. *J. Phys. Chem. B* **2012**, *116*, 7154-7161.

(7) Furuta, Y.; Komeno, T.; Nakamura, T. Favipiravir (T-705), a Broad Spectrum Inhibitor of Viral RNA Polymerase. *Proc. Jpn. Acad., Ser. B, Phys. Biol. Sci.* Japan Academy **2017**, pp 449-463.

(8) Furuta, Y.; Gowen, B. B.; Takahashi, K.; Shiraki, K.; Smee, D. F.; Barnard, D. L. Favipiravir (T-705), a Novel Viral RNA Polymerase Inhibitor. *Antivir. Res*. **2013**, pp 446-454.

(9) Tomita, Y.; Takeda, M.; Matsuyama, S. The Anti-Influenza Virus Drug Favipiravir Has Little Effect on Replication of SARS-CoV-2 in Cultured Cells. *Antimicrob. Agents Chemother.* **2021**, *65*.

(10) Cai, L.; Sun, Y.; Song, Y.; Xu, L.; Bei, Z.; Zhang, D.; Dou, Y.; Wang, H. Viral Polymerase Inhibitors T-705 and T-1105 Are Potential Inhibitors of Zika Virus Replication. *Arch. Virol.* **2017**, *162*, 2847-2853.

(11) Huchting, J.; Vanderlinden, E.; Winkler, M.; Nasser, H.; Naesens, L.; Meier, C. Prodrugs of the Phosphoribosylated Forms of Hydroxypyrazinecarboxamide Pseudobase T-705 and Its De-Fluoro Analogue T-1105 as Potent Influenza Virus Inhibitors. *J. Med. Chem.* **2018**, *61*, 6193-6210.

(12) Gowen, B. B.; Wong, M. H.; Jung, K. H.; Smee, D. F.; Morrey, J. D.; Furuta, Y. Efficacy of Favipiravir (T-705) and T-1106 Pyrazine Derivatives in Phlebovirus Disease Models. *Antiviral. Res.* **2010**, *86*, 121-127.

(13) Hillen, H. S.; Kokic, G.; Farnung, L.; Dienemann, C.; Tegunov, D.; Cramer, P. Structure of Replicating SARS-CoV-2 Polymerase. *Nature* **2020**, *584*, 154-156.

(14) Yin, W.; Mao, C.; Luan, X.; Shen, D. D.; Shen, Q.; Su, H.; Wang, X.; Zhou, F.; Zhao, W.; Gao, M.; Chang, S.; Xie, Y. C.; Tian, G.; Jiang, H. H. W.; Tao, S. C.; Shen, J.; Jiang, Y.; Jiang, H. H. W.; Xu, Y.; Zhang, S.; Zhang, Y.; Xu, H. E. Structural Basis for Inhibition of the RNA-Dependent RNA Polymerase from SARS-CoV-2 by Remdesivir. *Science.* **2020**, *368*, 1499-1504.

(15) Kaptein, S. J. F.; Jacobs, S.; Langendries, L.; Seldeslachts, L.; ter Horst, S.; Liesenborghs, L.; Hens, B.; Vergote, V.; Heylen, E.; Barthelemy, K.; Maas, E.; de Keyzer, C.; Bervoets, L.; Rymenants, J.; van Buyten, T.; Zhang, X.; Abdelnabi, R.; Pang, J.; Williams, R.; Thibaut, H. J.; Dallmeier, K.; Boudewijns, R.; Wouters, J.; Augustijns, P.; Verougstraete, N.; Cawthorne, C.; Breuer, J.; Solas, C.; Weynand, B.; Annaert, P.; Spriet, I.; Velde, G. Vande; Neyts, J.; Rocha-Pereira, J.; Delang, L. Favipiravir at High Doses Has Potent Antiviral Activity in SARS-CoV-2−infected Hamsters, Whereas Hydroxychloroquine Lacks Activity. *Proc. Natl. Acad. Sci. U. S. A.* **2020**, *117*, 26955-26965.

(16) Jockusch, S.; Tao, C.; Li, X.; Anderson, T. K.; Chien, M.; Kumar, S.; Russo, J. J.; Kirchdoerfer, R. N.; Ju, J. A Library of Nucleotide Analogues Terminate RNA Synthesis Catalyzed by Polymerases of Coronaviruses Causing SARS and COVID-19. *bioRxiv*. **2020**.

(17) Quintal, S.; Pires da Silva, M. J.; Martins, S. R. M.; Sales, R.; Felix, V.; Drew, M. G. B.; Meireles, M. M.; Mourato, A.; Nunes, C. D.; Saraiva, M. S.; Machuqueiro, M.; Calhorda, M. J. Molybdenum(II) Complexes with p-Substituted BIAN Ligands: Synthesis, Characterization, Biological Activity and Computational Study. *Dalt. Trans.* **2019**.

(18) Casadevall, A.; Pirofski, L. A. In Fatal COVID-19, the Immune Response Can Control the Virus but Kill the Patient. *Proc. Natl. Acad. Sci. U. S. A.* **2020**, *117*, 30009-30011.

(19) Hirouchi, T.; Ota, S.; Mashima, D.; Boku, R.; Yoshida, Y.; Iwata, K.; Shinada, K.; Matsumoto, T.; Morikawa, M.; Sato, T.; Shinoda, M.; Kamachi, K.; Shinkai, M. A Case of COVID-19 Pneumonia Successfully Treated with Favipiravir (Avigan) in Which Serum SARS-CoV-2 RNA Detected by LAMP Method Was Clinically Useful. *J. Infect. Chemother.* **2021**, *27*, 379-383.

(20) Weigert, A.; von Knethen, A.; Fuhrmann, D.; Dehne, N.; Brüne, B. Redox-Signals and Macrophage Biology. *Mol. Aspects Med.* **2018**, *63*, 70-87.

(21) Agita, A.; Alsagaff, M. T. Inflammation, Immunity, and Hypertension. *Acta Med. Indones.* **2017**, *49*, 158-165.

(22) Muri, J.; Kopf, M. Redox Regulation of Immunometabolism. *Nat. Rev. Immunol.* **2021**, *21*, 363-381.

(23) Zhou, D.; Porter, W. R.; Zhang, G. G. Z. Drug Stability and Degradation Studies. In *Developing Solid Oral Dosage Forms: Pharmaceutical Theory and Practice: Second Edition*; Elsevier Inc., **2017**; pp 113-149.

(24) Nanni, E. J.; Birge, R. R.; Hubbard, L. M.; Morrison, M. M.; Sawyer, D. T. Oxidation and Dismutation of Superoxide Ion Solutions to Molecular Oxygen. Singlet vs. Triplet State. *Inorg. Chem.* **1981**, *20*, 737-741.

(25) Nanni, E. J.; Stallings, M. D.; Sawyer, D. T. Does Superoxide Ion Oxidize Catechol, α-Tocopherol, and Ascorbic Acid by Direct Electron Transfer? *J. Am. Chem. Soc.* **1980**, *102*, 4481-4485.

(26) Song, C.; Zhang, J. Electrocatalytic Oxygen Reduction Reaction. In *PEM Fuel Cell Electrocatalysts and Catalyst Layers: Fundamentals and Applications*; **2008**; pp 89-134.

(27) Singh, P. S.; Evans, D. H. Study of the Electrochemical Reduction of Dioxygen in Acetonitrile in the Presence of Weak Acids. *J. Phys. Chem. B* **2006**, *110*, 637-644.

(28) Nakayama, T.; Uno, B. Concerted Two-Proton-Coupled Electron Transfer from Catechols to Superoxide via Hydrogen Bonds. *Electrochim. Acta* **2016**, *208*, 304-309.

(29) Nakayama, T.; Uno, B. Quinone-Hydroquinone π-Conjugated Redox Reaction Involving Proton-Coupled Electron Transfer Plays an Important Role in Scavenging Superoxide by Polyphenolic Antioxidants. *Chem. Lett.* **2010**, *39*, 162-164.

(30) Nakayama, T.; Uno, B. Importance of Proton-Coupled Electron Transfer from Natural Phenolic Compounds in Superoxide Scavenging. *Chem. Pharm. Bull. (Tokyo).* **2015**, *63*, 967-973.

(31) Nakayama, T.; Uno, B. Structural Properties of 4-Substituted Phenols Capable of Proton-Coupled Electron Transfer to Superoxide. *Int. J. Adv. Res. Chem. Sci.* **2016**, *3*, 11-19.

(32) Biela, M.; Rimarčík, J.; Senajová, E.; Kleinová, A.; Klein, E. Antioxidant Action of Deprotonated Flavonoids: Thermodynamics of Sequential Proton-Loss Electron-Transfer. *Phytochemistry* **2020**, *180*.

(33) Fridovich, I. Superoxide Dismutase. In *Encyclopedia of Biological Chemistry: Second Edition*; Elsevier Inc., **2013**; pp 352-354.

(34) Nakayama, T.; Honda, R. Electrochemical and Mechanistic Study of Superoxide Elimination by Mesalazine through Proton-Coupled Electron Transfer. *Pharmaceuticals* **2021**, *14*.

(35) Nakayama, T.; Okumura, N.; Uno, B. Complementary Effect of Intra- and Intermolecular Hydrogen Bonds on Electron Transfer in β–Hydroxy-Anthraquinone Derivatives. *J. Phys. Chem. B* **2020**, *124*, 848-860.

(36) Okumura, N.; Uno, B. Electronic Spectra of the Electrogenerated 1,4-Benzoquinone π-Dianion and the Strongly Hydrogen-Bonded Charge-Transfer Complex with Methanol. *Bull. Chem. Soc. Jpn.* **1999**, *72*, 1213-1217.

(37) Katsumi, J.; Nakayama, T.; Esaka, Y.; UNO, B. Mechanistic Study on the Electrochemical Reduction of 9,10-Anthraquinone in the Presence of Hydrogen-Bond and Proton Donating Additives. *Anal. Sci.* **2012**, *28*, 257-265.

(38) Frisch G. W.; Schlegel, H. B.; Scuseria, G. E.; Robb, M. A.; Cheeseman, J. R.; Scalmani, G.; Barone, V.; Petersson, G. A.; Nakatsuji, H.; Li, X.; Caricato, M.; Marenich, A. V.; Bloino, J.; Janesko, B. G.; Gomperts, R.; Mennucci, B.; Hratch, D. J., M. J. T. Gaussian 16, Rev. B.01. *Gaussian, Inc., Wallingford, CT* **2016**.

(39) Glendening, E. D.; Landis, C. R.; Weinhold, F. Natural Bond Orbital Methods. ***Wiley*** *Interdiscip. Rev. Comput. Mol. Sci*. **2012**, *2,* 1-42.

For Table of Contents Only